Open Ceramics 9 (2022) 100248

Contents lists available at ScienceDirect

Open Ceramics

journal homepage: www.sciencedirect.com/journal/open-ceramics

Performance study of asymmetric oxygen transport membranes with vertically channelled pores by phase inversion tape casting

Yang Liu [a,b], Kai Wilkner [a,b,c], Unoaku Victoria Unije [a,b], Stefan Baumann [a,b,*], Robert Mücke [a,b], Falk Schulze-Küppers [a,b], Olivier Guillon [a,b,c]

[a] Forschungszentrum Jülich GmbH, Institute of Energy and Climate Research, IEK-1: Materials Synthesis and Processing, D-52428, Jülich, Germany
[b] Jülich Aachen Research Alliance: JARA-Energy, Germany
[c] RWTH Aachen University, Institute of Mineral Engineering Department of Ceramics and Refractory Materials, D-52064, Aachen, Germany

ARTICLE INFO

Keywords:
Phase inversion tape casting
Channelled pores
Permeation rate
Oxygen transport membranes

ABSTRACT

Asymmetric oxygen transport membranes have been extensively studied revealing the importance of the support porosity. In this study, asymmetric membranes with vertically channelled pores were prepared from $Ba_{0.5}Sr_{0.5}(Co_{0.8}Fe_{0.2})_{0.97}Zr_{0.03}O_{3-\delta}$ (BSCF-Z) by phase inversion tape casting. The rate-limiting effects of the membrane layer thickness, the support structure, and the activation layers were thoroughly analysed. This entails comparing the permeation rate of the samples with the membrane layer on different sides of the channelled supports. Pore tortuosity and computed permeability were evaluated from 3D-X-ray computed tomography and compared to previously reported asymmetric membranes prepared by tape-casting and freeze-drying. Due to a lower pore tortuosity, the channelled supports have an advantage in gas transport over the tape cast and freeze cast supports. However, this is compensated by a thicker membrane layer (~54 μm) resulting in similar performance compared to the thinner membrane layers (~20 μm) with freeze cast and tape cast supports.

1. Introduction

Ceramic oxygen transport membranes (OTMs) exhibiting mixed ionic and electronic conductivity (MIEC), have been extensively studied for a range of applications, for instance for separation of pure oxygen, or in membrane reactors directly consuming the separated oxygen in chemical reactions such as partial oxidation of methane to syngas (POM) or oxidative coupling of methane to higher hydrocarbons (ethylene and/or ethane) (OCM) [1–4]. Numerous methods such as the development of new materials to obtain a high ambipolar conductivity [5–11], the application of a catalytic surface to boost the surface exchange [12–14], the modification of membrane architectures [15–20], have been investigated as ways to improve oxygen permeability of OTMs. Reducing the thickness of the dense membrane increases the flux but yields a reduced mechanical stability. Therefore, the thin dense membrane need a porous support to gain sufficient mechanical stability. However, the porous support does not only provide mechanical strength for the membrane layer, but it also adds another transport resistance compared to a free-standing membrane due to different gas diffusion/convection mechanisms in the porous structure. This additional resistance can be fully rate-determining. Schulze-Küppers et al. recently showed, that using several materials with very different permeability showed identical performance when processed into thin supported membrane layers with similar microstructure [21]. Depending on the fabrication route [22], such as tape casting [17,23,24], freeze casting [25–28], and phase inversion [29–31], the porous supports have different pore morphologies with dispersed and connected pores, interconnected, aligned lamellar pores, and channelled pores, respectively. Among them, channelled pores prepared by the phase inversion method are expected to show an improved oxygen permeation rate, since the pore channels typically show very low tortuosity as well as large diameters [32]. In the phase inversion method, a slurry consisting of binder, solvent, additive, and ceramic powder is cast on a solid plate or extruded through a die, and then subsequently immersed in a non-solvent bath. Precipitation occurs when the solvent in the polymer solution is exchanged for water acting as non-solvent. Generally, porous ceramic membranes prepared with the phase inversion method contain three kinds of pores: sponge-like pores, finger-like pore channels, and the skin layer [33]. The

* Corresponding author. Forschungszentrum Jülich GmbH, Institute of Energy and Climate Research, IEK-1: Materials Synthesis and Processing, D-52428, Jülich, Germany
E-mail address: s.baumann@fz-juelich.de (S. Baumann).

https://doi.org/10.1016/j.oceram.2022.100248
Received 9 December 2021; Received in revised form 22 February 2022; Accepted 16 March 2022
Available online 23 March 2022

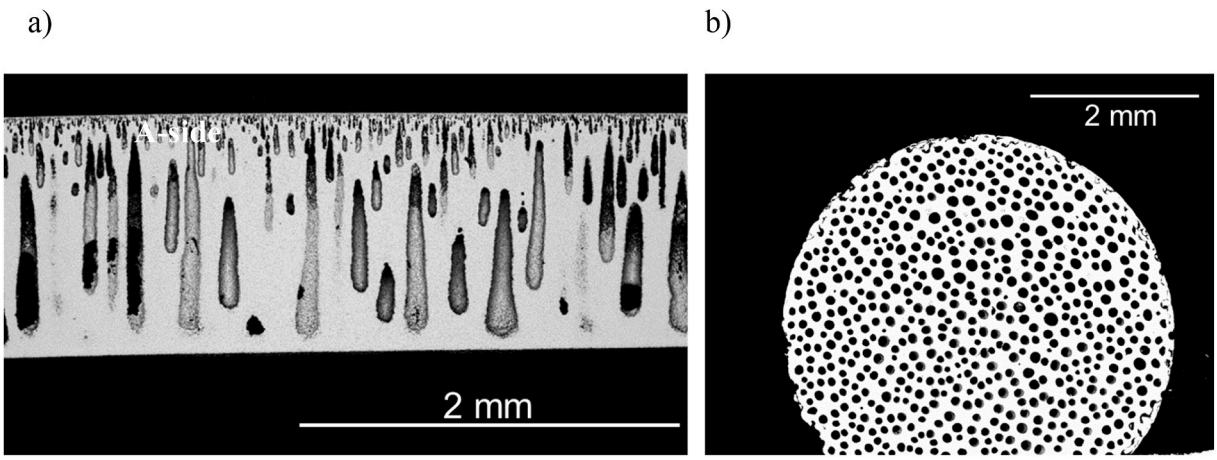

Fig. 1. SEM images showing (a) the cross-sections of the A side and the G-side of the prepared phase inversion tape cast sample, (b) cross section (paralle to A-side) of the porous support.

Skin layer and finger-like pores are results of rapid precipitation, and the sponge-like region is the result of delayed precipitation. The influence of fabrication parameters, as well as the solvent effects and compositions on pore morphologies of ceramic supports using the phase inversion method were studied [28,34]. For instance, Tan et al. [16] obtained a gastight LSCF hollow fiber membranes by the phase inversion method. Othman et al. [35] achieved a high oxygen permeability of the hollow fiber membrane reactor with thinner layers of separation and more open conical-shaped micro-channels by employing the phase inversion method. Open pore structured supports were prepared with the phase inversion tape casting method by removing the skin layers using graphite containing slurry [36] or steel mesh [37]. Furthermore, the influence of membrane thickness and surface limitation of the channelled pore supported asymmetric membranes were discussed by Zhang et al. [38].

In this work, channel pore structured supported planar asymmetric membranes were prepared by phase inversion method using $Ba_{0.5}Sr_{0.5}(Co_{0.8}Fe_{0.2})_{0.97}Zr_{0.03}O_{3-\delta}$ (BSCF-Z) materials. The parent material $Ba_{0.5}Sr_{0.5}Co_{0.8}Fe_{0.2}O_{3-\delta}$ (BSCF) is the material with the highest mixed ionic electronic conductivity (MIEC) so far [24,39–41]. Substitution with 3 mol% of Zr at the B-site stability issues of BSCF can be partly suppressed [42–44]. These properties make BSCF-Z a perfect candidate for this study. The high oxygen permeability minimizes the bulk diffusion resistance uncovering bottlenecks caused by e.g. the support microstructure, which might be negligible when using a low performing material. Moreover, the same BSCF-Z powder batch was used previously [15] investigating asymmetric membranes prepared by freeze-drying and tape casting enabling fair comparison of the different microstructures. As such, this research aims to gain new and in-depth insight into the bulk diffusion and the support and surface exchange limitations of the channel pore supported asymmetric membranes by varying the membrane layer thickness, support porosity and morphology, and adding an activation layer on the membrane surface, respectively. Furthermore, computed permeability of the pure supports without membrane layers, based on 3D-XCT of the supports, was carried out. The influence of pore morphology on permeation rates is discussed by comparing both, the simulated and experimental results, of phase inversion samples with freeze cast and tape cast samples, which are already reported in our previous study [15]. The phase inversion process applied here led to pore channels with much higher diameter and lower tortuosity compared to freeze-drying and tape casting and, thus, give promise in lowering the support resistance.

2. Experimental

2.1. Membrane fabrication

Polyethersulfone (PES, Ultrason, 6020P, BASF, Germany), 1-Methyl-2-pyrrolidone (NMP, 99.5 wt%, Sigma-Aldrich, Germany) and polyvinylpyrrolidone (PVP, K30 MW 40,000, Sigma-Aldrich, Germany) were used as polymeric binders, solvent, and additives, respectively. Commercial ceramic powder $Ba_{0.5}Sr_{0.5}(Co_{0.2}Fe_{0.8})_{0.97}Zr_{0.03}O_{3-\delta}$ (BSCF-Z) containing dense, compact particles was provided by Treibacher Industrie AG, Austria, and used to prepare the ceramic membranes. The BSCF-Z powders exhibit a monomodal particle size distribution with d_{10} ~1.7 μm, d_{50} ~3.6 μm and d_{90} ~5.9 μm as determined by dynamic light scattering (Horiba LA 950V2) and a specific surface area of 1.4 m^2/g determined by nitrogen adsorption (AreaMeter, Germany). Slurry with (NMP: PES: BSCF-Z = 2.8: 1: 8, weight ratio, 1.5 wt % PVP) was prepared. PES and PVP were added into the solvent NMP and stirred with a speed of 300 min^{-1} for 0.5 h. After the polymer fully dissolved into the solvent forming a homogeneous solution, BSCF-Z powder was slowly added into the solution. Afterwards, the slurry was stirred with a speed of 300 min^{-1} for 24 h by use of an electric lab mixer. The prepared homogenous slurry was first degassed in a vacuum for 1h. After that, the slurry was tape cast with approx. 10 mm/s on a glass substrate with a certain thickness controlled by a doctor blade. Then, the cast slurry was immediately immersed into water for the phase inversion. After 24 h, the phase inversion supports were dried in air for 48 h.

The dense membrane layers on porous supports were prepared by repeated screen printing using polyester screens (Koenen GmbH, Germany, Frame Type II) with different screen fineness, i.e. 12-140 and 45–70 leading to theoretical wet film thicknesses of 175 μm and 52 μm, respectively. Gas tight membranes were successfully obtained after sintering at 1130 °C for 10 h. The heating rate was set to 1K/min from 200 °C to 600 °C to slowly burn out the polymer, and 5 K/min to sintering temperature.

A porous activation catalytic layer of BSCF-Z was screen printed over the dense membrane surface. The used inks consisted of the same BSCF-Z powder as the membrane and the support layer, as well as a solvent/binder additive (94% terpineol, 6% ethylene cellulose). The screen printed layer (wet film thickness = 20 μm) was dried at 80 °C and calcined at 1000 °C obtaining a porous BSCF-Z catalytic layer of ~5 μm.

Dense membranes of 1.3 mm thickness were prepared by dry pressing of BSCF-Z powders in a mould (20 mm diameter) with 25 kN force pressure, for 2 min. The pressed samples were sintered at 1130 °C for 10 h with 5 K/min heating and cooling rates.

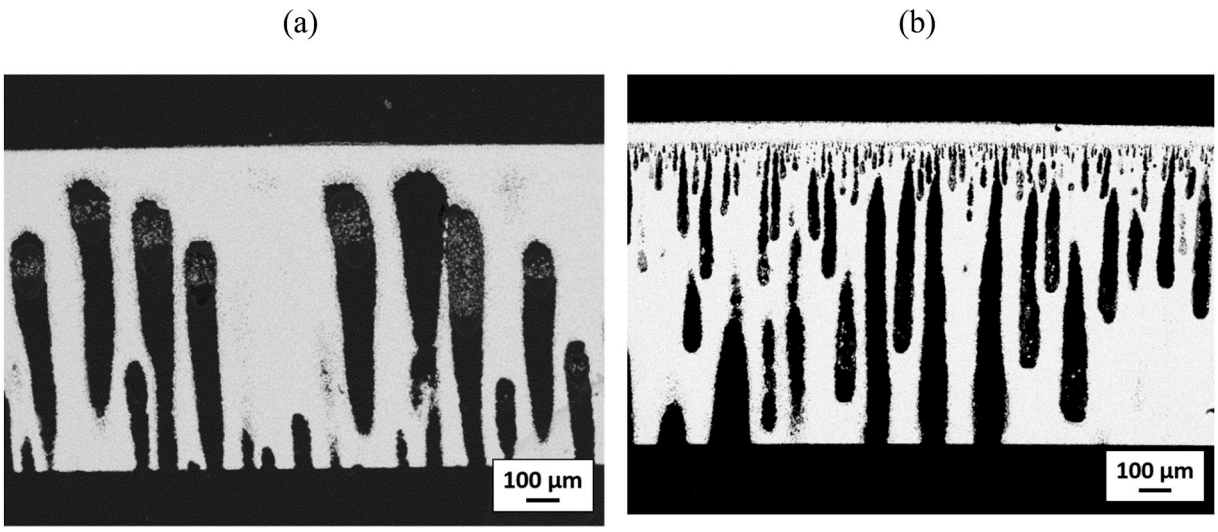

Fig. 2. cross sections of the two series of asymmetric membranes a) membrane layer on G-side, b) membrane layer on A-side.

Table 1
Thickness of the G-side, and A-side membranes, porosity of G-side support was 37% ± 2%, A-side support was 36% ± 1%

Sample	Total thickness (µm)	Membrane thickness (µm)	Support thickness (µm)
G71	965 ± 2	71 ± 15	886 ± 25
G163	1060 ± 11	163 ± 34	908 ± 21
G235	1015 ± 3	235 ± 17	775 ± 11
G67, ~5 µm act	992 ± 3	67 ± 20	921 ± 25
A55	1012 ± 2	55 ± 2	951 ± 5
A123	1043 ± 2	123 ± 2	915 ± 3
A223	941 ± 3	223 ± 5	719 ± 4
A54, ~5 µm act	985 ± 3	54 ± 3	925 ± 4

2.2. Microstructure analysis

Scanning electron microscopy (SEM) images of the polished membrane cross sections were taken using a FEI Phenom (FEI, The Netherlands). The commercial software analySIS pro (Olympus Soft Imaging Solutions GmbH, Germany) was used to analyze the thicknesses and porosities on the SEM images of the BSCF-Z membranes after permeation measurements. A 3D microstructure analysis of the BSCF-Z cylindrical sample with a diameter of 1.0 mm and a height of 1.0 mm was carried out by the X-ray computed tomography (XCT) (Zeiss Versa 420 nano, Germany) and analysed using the software GeoDict (Math2-Market GmbH, Germany).

2.3. Permeation rate test

Oxygen permeation measurements of disc-shaped membranes with a 14.7 mm diameter were conducted under an oxygen partial pressure gradient as the driving force, with the support at the feed side and the membrane at the sweep side. A constant flow rate of 250 mL min^{-1} ambient air or 200 mL min^{-1} of oxygen, respectively, and 50 mL min^{-1} of Ar were used as feed and sweep gas, respectively. The temperature varied from 650 °C to 1000 °C. Gold rings with an outer diameter of 15 mm and wire thickness of 1 mm were used to seal the samples to the gasket of the quartz glass reactor at approx. 1000 °C, resulting in an exposed membrane surface area of approx. 1.33 cm^2.

3. Results and discussion

3.1. Asymmetric membrane structure

The phase inversion tape cast (PI) supports show a channelled pore structure with a thin fine-porous skin layer on the air side (A-side) and a thick dense layer on the glass side (G-side), Fig. 1a. When the cast slurry is immersed into the water bath, the A-side slurry is exposed to the water, whereas the G-side is separated from the water due to the glass support. Thus the solvent NMP starts exchanging with the non-solvent, i.e. water, from the A-side reaching the precipation point immediately. In consequence, a skin layer forms at the A-side [45]. In succession, water penetrates deeply into the slurry and exchanges with the NMP, forming a polymer lean phase, i.e. NMP + water, with delayed precipitation inside the sample resulting in channelled pores after drying. Close to the G-side slow exchange of solvent and water leads to the formation of the thicker dense skin layer on G-side. The cross section in Fig. 1b shows the channels in the center of the sample revealing homogeneous distribution.

Asymmetric membranes with two systematically different microstructures were obtained.

One series of asymmetric membranes were prepared utilizing the thick dense layer on the G-side as membrane layer. For this purpose the A-side was ground removing the fine porous layer and, thus, opening the desired pore channels, Fig. 2a.

In the second series, the fine porous skin layer shall be utilized in order to increase the volume specific surface area at the interface of support and membrane layer. For this purpose, the thick dense G-side layer was removed by grinding. On top of the fine porous A-side layer a dense membrane layer was screen printed, Fig. 2b.

3.2. Asymmetric membrane performance

Several asymmetric membranes with the dense membrane layer on G-side and on the A-side, labelled as “G” and “A”, respectively, were prepared with different membrane layer thicknesses in order to investigate the relevant transport mechanisms in the different asymmetric structures. Membrane thicknesses varied between 71 µm, 163 µm, and 235 µm and 55 µm, 115 µm, and 223 µm for G-side and A-side membrane layers, respectively, Table 1. The two thinnest membrane layers were additionally coated with a porous surface activation layer of ~5 µm thickness.

However, the support thickness could not be kept constant, Table 1. It should be noted that the determination of membrane and support

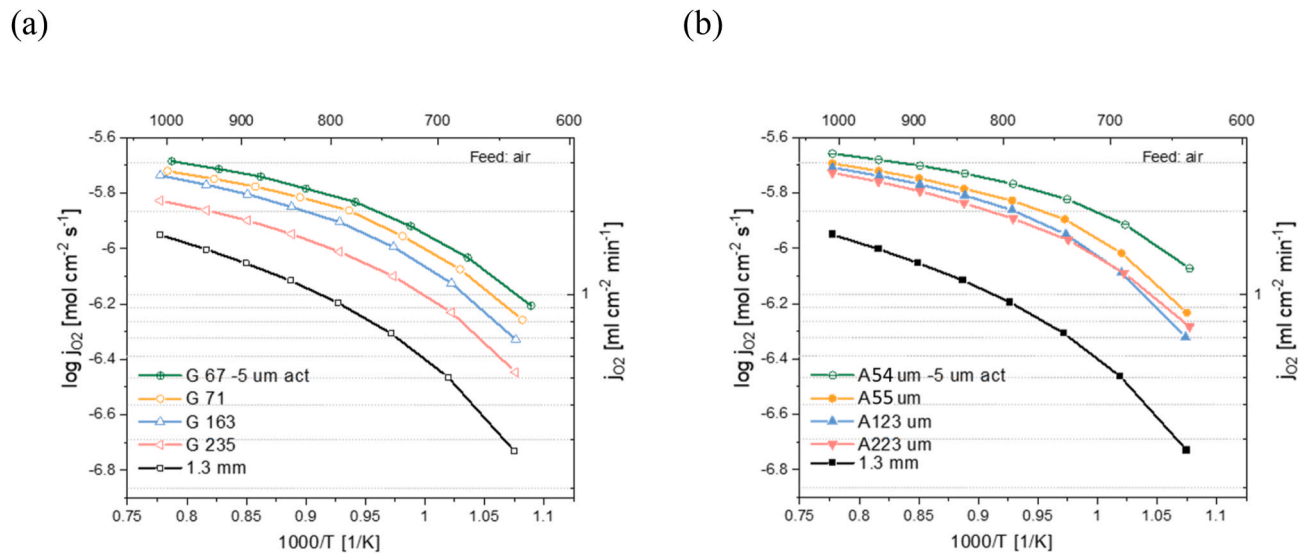

Fig. 3. Oxygen permeation rate of (a) G-side samples and (b) A-side samples, respectively, using air as feed gas towards the support layer and Ar as sweep gas towards the membrane layer.

Table 2
Activation energy of the oxygen permeation rates shown in Fig. 3 and

	E_a(kJ/mol) Feed air		E_a(kJ/mol) Feed oxygen	
Samples	800–1020 °C	650–750 °C	800–1020 °C	650–750 °C
Bulk 1.3 mm	47	105	/	/
G235	23	64	38	75
G163	21	62	41	66
G71	18	58	36	64
G67, ~5 μm act	18	54	36	59
A223	21	59	36	63
A123	19	71	35	78
A55	17	63	34	74
A54, ~5 μm act	14	46	32	55

thicknesses by microscopy of cross-sections, e.g. Fig. 2, is much easier in case of A-side samples, where the interface of the coated membrane layer and the support is well defined. In contrast, the end of the pore channels typically are not visible in such random cuts. Therefore, the distances of the pore channels to the membrane surfaces was measured for 10 times and the averages are considered as the membrane and support layer thicknesses, respectively. The natural uncertainty of this method results in a relatively high standard deviation given in Table 1. Nevertheless, the support thicknesses are in a relatively narrow range except for the two thickest membrane layers, i.e. G235 and A 223. Due to the high transport resistance in the membrane layer the support influence is expected to be minor in those cases. Therefore, the permeation results are considered to be representative for the membrane layer thicknesses. The oxygen permeation rate of the G-side and A-side samples, respectively, with varying membrane thickness using air as feed gas is plotted in Fig. 3.

The permeation rate of the G71 sample was nearly 2 times higher than the 1.3 mm thick bulk BSCF-Z disc at 900 °C due to the thinner membrane layer. As expected, the enhancement is not proportional to the reciprocal membrane layer thickness. This can be attributed to the fact that the solid state diffusion through the membrane layer is not solely limiting the overall transport. The apparent activation energies E_A^{app} of the oxygen permeation rate are listed in Table 2.

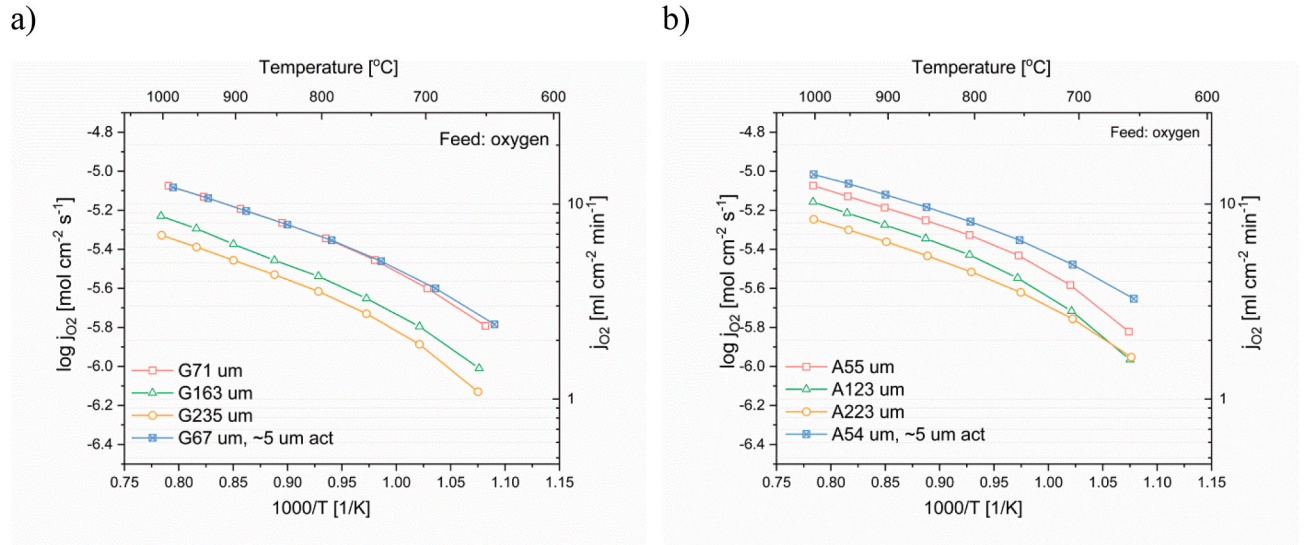

Fig. 4. Oxygen permeation rate of (a) G-side samples and (b) A-side samples, respectively, using oxygen as feed gas towards the support layer and Ar as sweep gas towards the membrane layer.

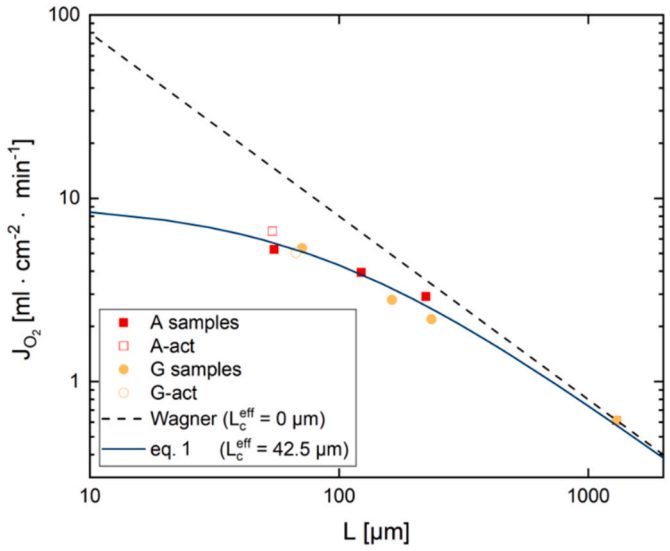

Fig. 5. Permeance J_{O2} versus thickness of A-side and G-side samples at 900 °C with oxygen feed.

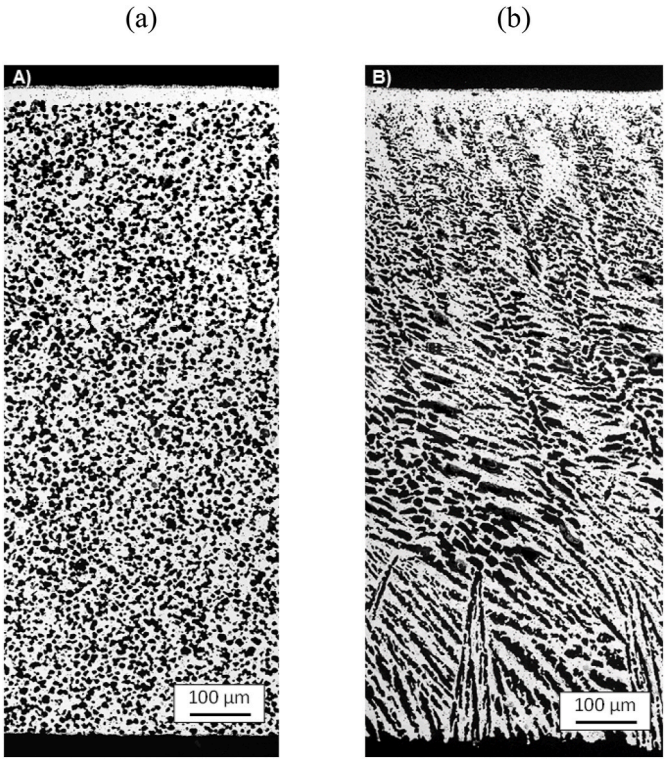

Fig. 6. Cross sections of asymmetric membranes prepared by a) tape casting and b) freeze drying. Reproduced with permission [15]. Copyright 2018, Elsevier.

The pressed disc sample with 1.3 mm thickness can be used as a reference because the solid state diffusion is the rate determining step compared to surface exchange and gas phase polarizations at high temperature, i.e. ≥ 800 °C. The corresponding E_A^{app} = 47 kJ/mol is in very good agreement to literature values of the parent material BSCF [15,17]. At lower temperature E_A^{app} is higher attributed to an increased influence of sluggish surface exchange kinetics with an E_A = 1.6 eV (~154 kJ/mol) in case of the parent material BSCF [46]. In contrast, a lower E_A^{app} indicates a significant contribution of gas phase processes [24]. This is observed in particular in asymmetric membranes at high temperatures, where gas transport through the porous support can become fully rate limiting [21] easily showing an E_A^{app} as low as 10 kJ/mol.

At high temperature, i.e. ≥ 800 °C, E_A^{app} of both, G-side and A-side samples, is well below 47 kJ/mol indicating that the gas transport through the porous support contributes to the permeation rate limitation. Accordingly, E_A^{app} decreases with decreasing thickness because the enhanced mass transfer through the entire membrane assembly further increases the fraction of support transport resistance. At lower temperatures, i.e. 650-750 °C, E_A^{app} still is much less compared to the thick membrane disc in all cases. However, it strongly increases compared to the high temperature range indicating a decreasing fraction of support resistance due to the lower overall flux. In consequence, bulk diffusion and surface exchange play an increasing role in the permeation rate limitation.

For the G-side membrane the porous surface activation layer on the membrane layer, i.e. permeate side, does not influence both the oxygen permeation rate as well as E_A^{app} over the entire temperature range revealing no significant influence of surface exchange at the permeate side. This might be attributed to a low volume specific surface area at that interface as indicated in Fig. 2a leading to more sluggish surface exchange at the feed side. In contrast, for the A-side membrane the permeation rate and the E_A^{app} clearly increases and decreases, respectively, in particular at the lower temperature region indicating that the surface exchange limitation at the permeate side is not negligible. This is in accordance with the concept utilizing the fine porous layer originating from the phase inversion process as a potential surface activation layer at the support-membrane interface, Fig. 2b).

When pure oxygen is used as feed gas, cf. Fig. 4, the concentration polarization in the porous support is eliminated resulting in a significantly enhanced permeation rate due to the much lower support transport resistance. In consequence, the E_A^{app} increases coming close to the reference value for bulk diffusion of 47 kJ/mol in the high temperature region. For the G-side sample again the activation layer did not improve the permeation rate over the entire temperature range, implying the surface exchange at the permeate side still is not relevant. At high temperature, bulk diffusion might be dominating whereas at lower temperatures surface exchange at the support-membrane interface is expected to play a significant role. In contrast, the activation layer improves the performance of the A-side sample over the entire temperature range. This occurs in particular in the lower temperature region as expected. Nevertheless, E_A^{app} still is above the reference of 47 kJ/mol indicating that the surface exchange limitations are not completely overcome. The increased volume specific surface area at the support-membrane interface apparently has a positive effect on the performance, which would result in an increased role of the surface exchange at the permeate side in the overall transport limitation.

In order to further evaluate the thickness dependence of the asymmetric membranes, the measurements with oxygen as feed gas are used minimizing the support limitation. The modified Wagner equation introduced by Bouwmeester et al. [47] considers bulk diffusion and surface exchange by the characteristic thickness L_c.

$$j_{O2} = \frac{RT}{16F^2}\frac{1}{L+2L_c}\sigma_{amb}\ln\frac{p'_{O2}}{p''_{O2}} \quad (1)$$

with R = 8.314 J mol^{-1} K^{-1} gas constant, T [K] absolute temperature, F = 96485 C mol^{-1} Faraday constant, L [m] membrane layer thickness, L_c [m] characteristic thickness, σ_{amb} [S m^{-1}] ambipolar conductivity and p'_{O2} and p''_{O2} [bar] oxygen partial pressures in the retentate and permeate gas, respectively. It has to be noted that according to the derivation of Equation (1) L_c is a sole materials parameter, i.e. the ratio of oxygen self-diffusion coefficient D* [cm^2 s^{-1}] and surface exchange coefficient k_s [cm s^{-1}].

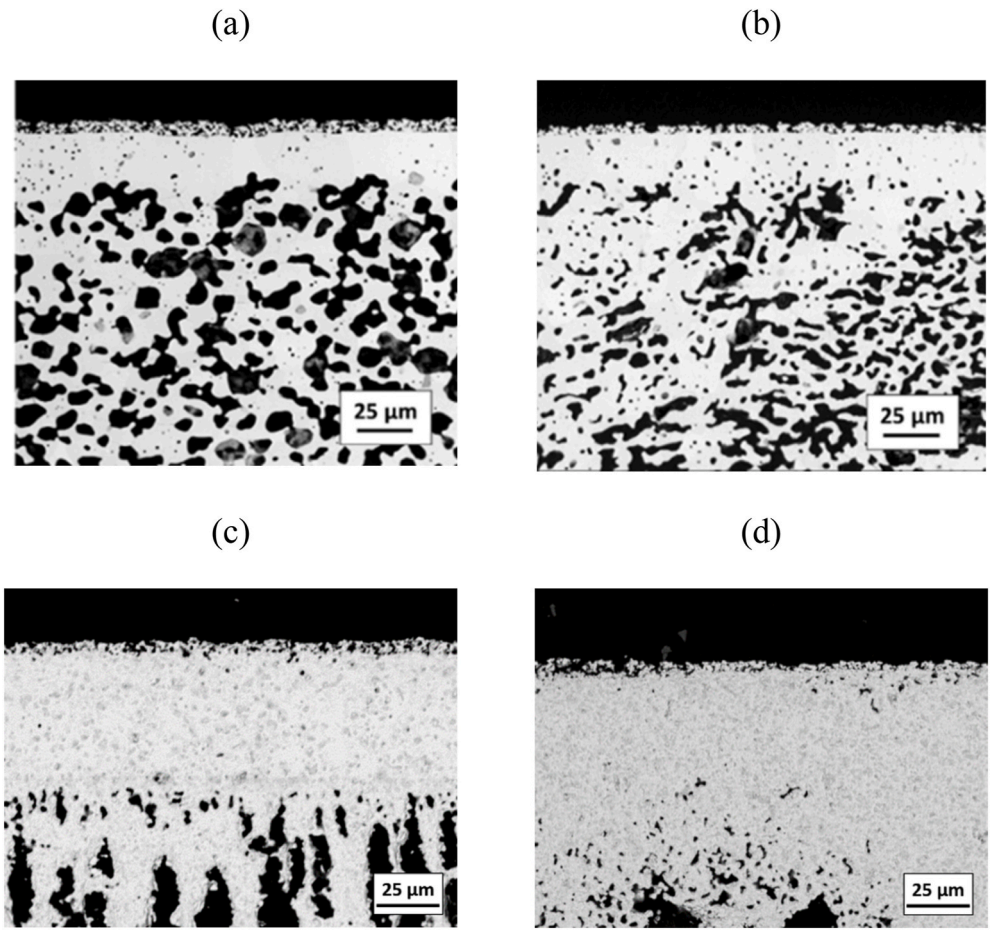

Fig. 7. SEM images of (a) TC and (b) FC samples [15] as well as (c) A54,~5 µm act and (d) G67, a ~5 µm thick porous activation layer is applied on all membrane layers.

Table 3
Microstructural parameters of the TC, FC, A side and G side samples. The porosities were calculated from the SEM images of the cross-section from 20 images.

Sample name	$L_{act.layer}$ [µm]	$L_{mem.layer}$ [µm]	$L_{support}$ [µm]	$\varepsilon_{support\text{-}mean}$ [%] porosity
G67, ~5 µm act	~5	67	921 ± 25	37 ± 2
A54, ~5 µm act	~5	54 ± 3	925 ± 4	36 ± 1
TC [15]	5–6	22–24	990	45.5 ± 1.8
FC [15]	4–5	22–24	990	45.5 ± 5.5

$$L_c = \frac{D^*}{k_s} \tag{2}$$

However, geometrical aspects such as surface roughness or porous coatings influence the actual surface exchange rate. We consider this by introducing the term effective characteristic thickness L_c^{eff}, which can be derived by fitting experimental data to Equation (1) provided that all other variables are kept constant, e.g. by isothermic operation. However, it needs to be considered that the driving force is not constant with varying membrane thickness. With lower thickness more oxygen permeates through the membrane and, thus, the p_{O2}'' increases due to constant Ar mass flow rates. On the other hand p_{O2}' might decrease, however, typically it does not change significantly if air flow rates are high enough or pure oxygen is used as feed gas. In consequence, the driving force decreases with increasing permeation rates resulting from decreased thickness.

Therefore, the permeance J_{O2} [mol cm^{-2} s^{-1}], i.e. the permeation rate normalized by the driving force, is used to analyze the thickness dependence of the asymmetric membranes at a constant temperature.

$$J_{O2} = \frac{j_{O2}}{\ln \frac{p'_{O2}}{p''_{O2}}} \tag{3}$$

Fig. 5 shows the double logarithmic plot of the permeance versus the membrane thickness. The 1.3 mm thick disc was used to calculate the dashed line representing the Wagner behaviour, i.e. pure solid state diffusion with $L_c^{eff} = 0$ µm, which can be considered as upper bound for the permeance. The thinner the membrane layer, the larger is the deviation from this upper bound since surface exchange becomes more and more dominant. The solid line represents Equation (1) with $L_c^{eff} = 42.5$ µm resulting from a fit through all data points, which is equal to reported data for the parent material BSCF [48,49]. Obviously, all sets of experiments, i.e. A-side and G-side both with and without surface activation layer, fit this curve quite well. The individually fitted L_c^{eff} for each set does not change significantly and, thus, the accordant lines are not shown in Fig. 5. It varies between 40.5 µm and 45.5 µm for A-side and G-side, respectively, indicating that the fine porous layer at the membrane-support interface existing in the A-side samples facilitates surface exchange at the feed side, though very limited, resulting in lower L_c^{eff} = 33.5 µm. In contrast, the surface activation layer is fully ineffective. Please note, that the fitting through such single measuring points has a high uncertainty and should not be overrated. Nevertheless, the results indicate a certain contribution of the permeate side surface exchange to the overall transport in case of A-side sample contrary to the G-side sample.

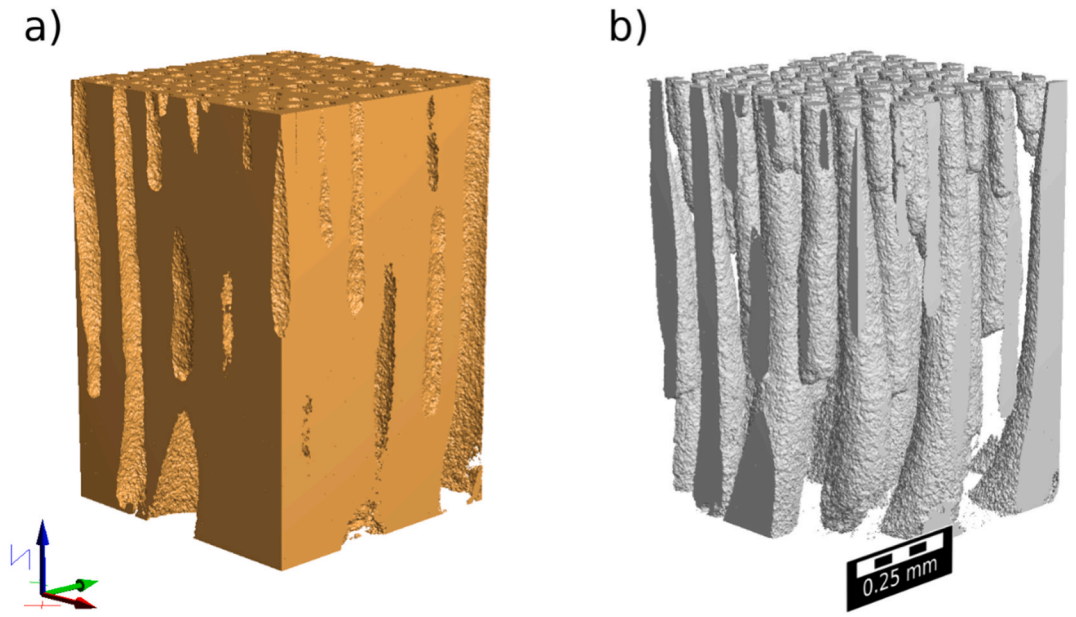

Fig. 8. Architecture of a phase inversion tape casting (ITC) support, reconstructed from XCT data using GeoDict software. a) solid BSCF-Z phase b) fluid space (pores).

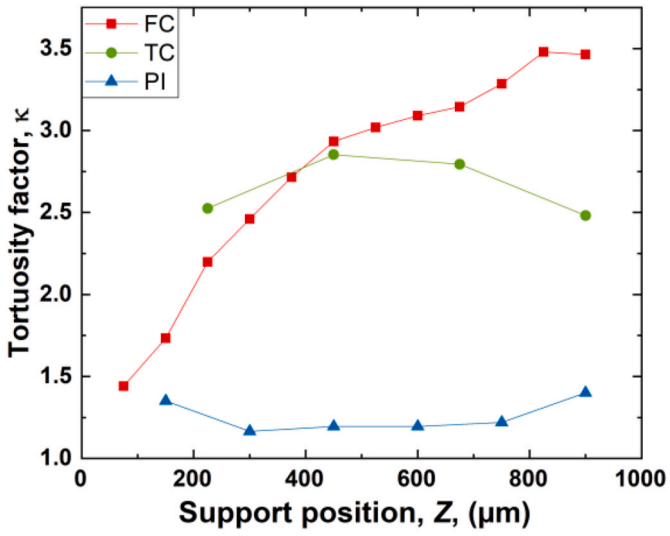

Fig. 9. Evaluation of tortuosity factor ($\kappa = \tau^2$) plotted vs. section position (y-coordinate); the position of the support-membrane interface is at Z = 1000 μm in case of FC, TC, and A-side PI and at Z = 0 μm in case of G-side PI.

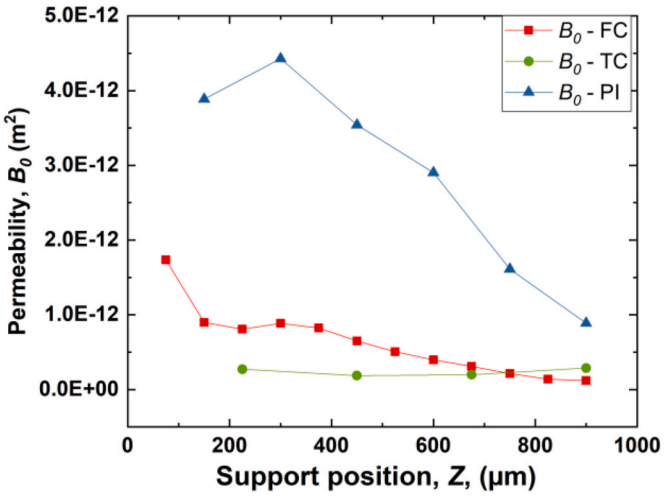

Fig. 10. Computed permeability (B_0) plotted vs. section position (y-coordinate); the position of the support-membrane interface is at Z = 1000 μm in case of FC, TC and A-side PI, and at Z = 0 μm in case of G-side PI.

Concluding, the fine porous region at the support-membrane interface of the A-side samples might have the potential facilitating surface exchange. But in this particular case it is not very significant because the minimum membrane layer thickness is 54 μm and 67 μm for A-side and G-side samples, respectively. Moreover, pure oxygen is used as feed gas enhancing the surface exchange rate compared to feeding air, because it is p_{O2}-dependent following a power law, i.e. $k_s \approx p_{O2}^n$ [50,51]. At the permeate side, the very thin surface activation layer does not provide very much additional surface area and, thus, is expected to be effective only if the surface exchange limitations are dominating, i.e. thinner membrane layers are achieved.

3.3. Comparison of supports with systematically different microstructures

To further evaluate the porous supports achieved in this work using the phase inversion process (PI), simulated and experimental results were compared with asymmetric membranes prepared by tape casting (TC) and freeze casting (FC), respectively, reported in a previous paper [15], Fig. 6. The pore distribution in TC samples appear isotropic, whereas the FC sample showed more aligned yet not optimized porosity. In contrast, the PI samples (Fig. 2) provides straight channels with very large diameters of up to 100 μm.

Fig. 7 shows a closer look to the microstructure at the membrane-support interface region revealing the lower thickness of TC and FC membrane layers and a very similar porous activation layer of approx. 5 μm thickness. Selected microstructural paramters are listed in (Table 3).

For further analysis X-Ray computed Tomography (XCT) was performed. The 3D-reconstruction is shown in.

Fig. 8 revealing the intended straight pore channels. In G-side samples the membrane layer is at the bottom side whereas in A-side samples the membrane layer is on top of this structure. In the latter case the presence of more pore channels with lower diameter is visible in

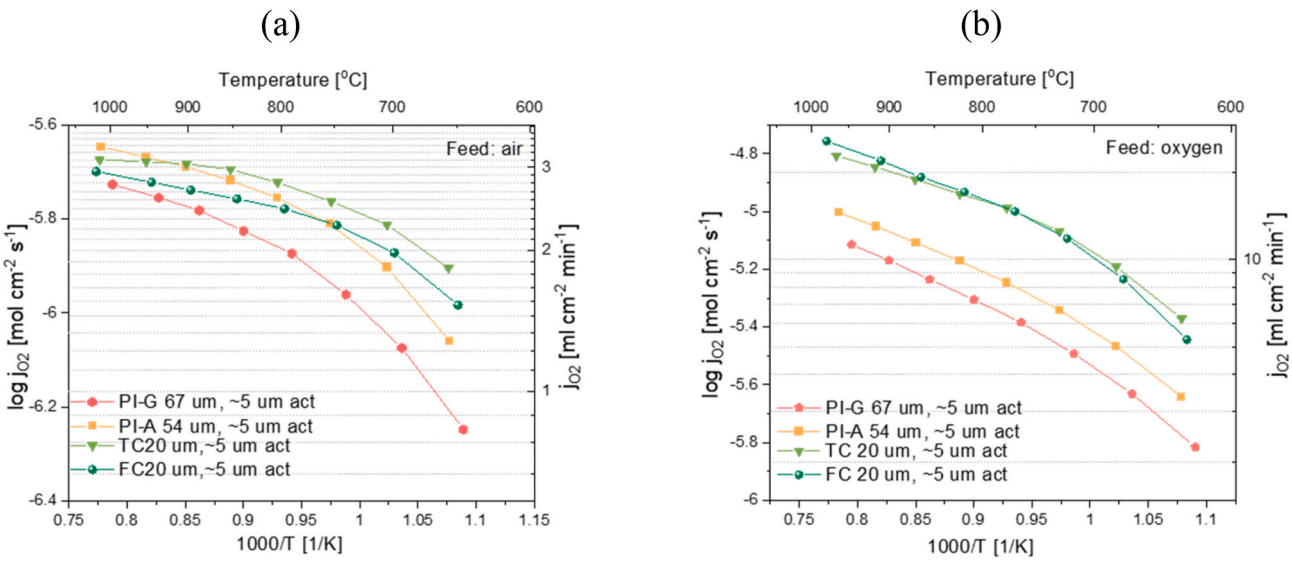

Fig. 11. Oxygen permeation rate of TC, FC, and PI samples feeding (a) air and (b) oxygen towards the support layer.

Table 4
Activation energy of bulk discs and PI samples as well as the TC and FC samples from [15].

Samples	Activation energy E_a [kJ/mol] Feed air		Activation energy E_a [kJ/mol] Feed oxygen	
	800–1050 °C	650–750 °C	800–1050 °C	650–750 °C
Bulk 1.3 mm	47	105	/	/
G67, ~5 μm act	18	54	36	59
A54, ~5 μm act	14	46	32	55
TC	6	27	24	55
FC	9	31	28	65

accordance with Fig. 2a/b and Fig. 7c/d. However, these pores seemingly are not well connected to each other and rather dead-end pores, thus, not significantly contributing to the overall performance. This feature is likely the reason, why A-side samples show only slightly better performance over G-side samples as shown in Fig. 5 and should attain more attention in future developments.

From the 3D reconstruction tortuosity τ and simulated permeability B_0 of the phase inversion support were evaluated. Simplified spoken, tortuosity describes the ratio of the path length of a molecule through a pore channel (L_{pore}) to the shortest length through the support ($L_{support}$).

$$\tau = \frac{L_{pore}}{L_{support}} \tag{4}$$

For the permeation process, the tortuosity factor ($\kappa = \tau^2$) is relevant, which is plotted in Fig. 9 confirming that the PI support has the desired much lower tortuosity factor compared to the previously reported TC and FC [15]. The tortuosity and, thus, tortuosity factor of the PI samples is close to unity throughout the entire sample, reflecting the desired straighter pores compared to the FC and TC supports.

The gas permeability B_0 represents the intrinsic permeability of the porous medium and can be computed via a virtual permeation test according to Darcy's law:

$$Q = \frac{-B_0 A}{\mu}\frac{\Delta p}{L} \tag{5}$$

where Q [m^3 s^{-1}] represents the permeation rate through a tube, A [m^2] the tube's cross-sectional area, Δp [Pa] the pressure drop, μ [Pa s] the viscosity of the gas, and L [m] the sample thickness.

The computed permeability B_0, plotted in Fig. 10, is more than double compared to that of the TC and FC supports at Z = 0 μm and an order of magnitude higher at Z = 1000 μm though decreasing approx. by a factor of 4. This result shows the high potential of the PI support regardless of the membrane layer position (Z = 0 μm or Z = 1000 μm) although the structure is not yet optimized in the particular case investigated here.

Fig. 11 shows the temperature dependent permeation rate of the PI samples (A54,~5 μm act and G67,~5 μm act) together with the TC and the FC samples with an activation layer as shown in Fig. 7.

When feeding air, the A54,~5 μm act presented a similar permeation rate as the TC and the FC at high temperature. The activation energy of A54,~5 μm act sample is higher, Table 4, which is related to the thicker membrane layer leading to a more significant contribution of solid state diffusion to the overall rate limitation. In consequence, the FC and in particular TC sample show superior permeation rates at lower temperatures, where the support influence is decreased due to lower overall performance. This phenomenon is based on the fact, that the support influence as such is dependent on the flux through the support and, thus, performance dependent. This back coupling makes the transport considerations so complex.

Feeding oxygen minimizes the influence of the porous supports and, thus, the activation energies of all samples are similar in particular at high temperatures indicating a major transport limitation by solid state diffusion. Therefore, the PI-samples show approx. 2 times lower permeation rates due to the much thicker membrane layers, i.e. 2.3 and 2.9 times thicker for A54,~5 μm act and G67,~5 μm act, respectively. As a consequence, if the same membrane thickness can be achieved on a PI support, the permeation rate can be expected to equal that of TC and FC when feeding oxygen and a superior performance when feeding air.

4. Conclusions

Asymmetric membranes with a channelled porous support made of $Ba_{0.5}Sr_{0.5}(Co_{0.8}Fe_{0.2})_{0.97}Zr_{0.03}O_{3-\delta}$ (BSCFZr) were prepared by a phase inversion method. Both microstructure and performance were investigated thoroughly. The results are compared to previously reported asymmetric membranes made from the same material using tape casting and freeze drying, respectively.

The phase inversion process leads to a fine porous skin layer. Applying the dense membrane layer on top of this skin layer leads to a slightly better performance compared to the membrane layer on the opposite side. This might be attributed to facilitated surface exchange kinetics at the support-membrane interface with potentially higher

surface area. However, assessing the membrane layer thickness dependence of the permeance reveals that the differences are not very significant. X-Ray Computed Tomography revealed that part of the finer pore channels are not connected to each other and, thus, represent dead-end pores apparently compensating the positive effect of higher surface area.

In general, the channels with very large pore diameters, i.e. ~100 μm, enables fast gas transport through the support reflected by much higher computed permeability B_0 compared to tape casting and freeze drying revealing high potential for asymmetric membranes. Nevertheless, at high temperatures and, thus, high permeation rates the support limitations are reduced though still considerable.

Since the membrane layers prepared in this work were thicker compared to the tape cast and freeze dried samples, the maximum permeation rates achieved in this study are rather similar. However, the results clearly show the potential of this support structure, i.e. large pore diameter and low tortuosity, if thinner membrane layers can be achieved. It has to be noted that such support structures are achievable by different techniques, e.g. phase inversion or freeze-drying. In any case, due to the strong interlinkage of the single resistors in an asymmetric membrane, i.e. bulk diffusion, surface exchange, and porous support, the actual support limitation is dependent on the overall performance. Therefore, the optimum microstructure of the porous support is dependent on all factors affecting the performance such as membrane material and operating conditions.

Another conclusion is that the thin porous activation layers applied on top of the membrane layers obviously are not effective. This is partly because surface exchange currently plays a minor role in the investigated conditions, i.e. relatively thick membrane layers and high oxygen partial pressures. But the activation layers will definitely need optimization if thinner membrane layers are achieved.

Declaration of competing interest

The authors declare that they have no known competing financial interests or personal relationships that could have appeared to influence the work reported in this paper.

Acknowledgement

Yang Liu is greatful to the China Scholarship Council (CSC) for providing financial support for this work. Kai Wilkner and Unoaku Unije acknowledges financial support by the Helmholtz Graduate School for Energy and Climate Research (HITEC) at Forschungszentrum Jülich GmbH. The authors thank Andreas Everwand (Forschungszentrum Jülich GmbH, IEK-14) for performing XCT measurement.

References

[1] J. Sunarso, S. Baumann, J.M. Serra, W.A. Meulenberg, S. Liu, Y.S. Lin, J.C. Diniz da Costa, Mixed ionic-electronic conducting (MIEC) ceramic-based membranes for oxygen separation, J. Membr. Sci. 320 (2008), https://doi.org/10.1016/j.memsci.2008.03.074.

[2] Z. Cao, H. Jiang, H. Luo, S. Baumann, W.A. Meulenberg, H. Voss, J. Caro, Simultaneous overcome of the equilibrium limitations in BSCF oxygen-permeable membrane reactors: water splitting and methane coupling, Catal. Today 193 (2012), https://doi.org/10.1016/j.cattod.2011.12.018.

[3] T. Chen, Z. Wang, L. Liu, S. Pati, M.H. Wai, S. Kawi, Coupling CO2 separation with catalytic reverse water-gas shift reaction via ceramic-carbonate dual-phase membrane reactor, Chem. Eng. J. 379 (2020), 122182, https://doi.org/10.1016/j.cej.2019.122182.

[4] K. Jiang, Z. Liu, G. Zhang, W. Jin, A novel catalytic membrane reactor with homologous exsolution-based perovskite catalyst, J. Membr. Sci. 608 (2020), 118213, https://doi.org/10.1016/j.memsci.2020.118213.

[5] W. Fang, F. Liang, Z. Cao, F. Steinbach, A. Feldhoff, A mixed ionic and electronic conducting dual-phase membrane with high oxygen permeability, Angew. Chem. Int. Ed. 54 (2015) 4847–4850, https://doi.org/10.1002/anie.201411963.

[6] Z. Dehaney-Steven, D. Papargyriou, J.T.S. Irvine, Flux investigations on composite (La0.8Sr0.2)0.95Cr0.5Fe0.5O3 - δ-Sc0.198Ce0.012Zr0.789O1.90 oxygen transport membranes, Solid State Ionics 288 (2016) 338–341, https://doi.org/10.1016/j.ssi.2016.01.017.

[7] Y. Lin, S. Fang, D. Su, K.S. Brinkman, F. Chen, Enhancing grain boundary ionic conductivity in mixed ionic-electronic conductors, Nat. Commun. 6 (2015) 6824, https://doi.org/10.1038/ncomms7824.

[8] Y. Liu, V. Motalov, S. Baumann, D. Sergeev, M. Müller, Y.J. Sohn, O. Guillon, Thermochemical stability of Fe- and co-functionalized perovskite-type $SrTiO_3$ oxygen transport membrane materials in syngas conditions, J. Eur. Ceram. Soc. 39 (2019), https://doi.org/10.1016/j.jeurceramsoc.2019.06.045.

[9] G. He, Q. Lan, Y.J. Sohn, S. Baumann, R. Dunin-Borkowski, W.A. Meulenberg, H. Jiang, Temperature-induced structural reorganization of W-doped $Ba_{0.5}Sr_{0.5}Co_{0.8}Fe_{0.2}O_3$-δ composite membranes for air separation, Chem. Mater. 31 (2019), https://doi.org/10.1021/acs.chemmater.9b02213.

[10] L.R. Tarutina, G.K. Vdovin, J.G. Lyagaeva, D.A. Medvedev, Comprehensive analysis of oxygen transport properties of a BaFe0.7Zr0.2Y0.1O3–δ-based mixed ionic-electronic conductor, J. Membr. Sci. 624 (2021), 119125, https://doi.org/10.1016/j.memsci.2021.119125.

[11] J. Shi, X. Zhu, K. Li, Y. Wei, H. Wang, Zr0.92Y0.08O1.92-La0.6Sr0.4Co0.2Fe0.8O3–δ asymmetric dual-phase oxygen transport membrane for simultaneously methane partial oxidation and water splitting, Fuel Cell. 21 (2021) 58–65, https://doi.org/10.1002/fuce.202000049.

[12] L. Hao, J. Yu, X. Xu, L. Yang, Z. Xing, Y. Dai, Y. Sun, J. Zou, Nitrogen-doped MoS2/carbon as highly oxygen-permeable and stable catalysts for oxygen reduction reaction in microbial fuel cells, J. Power Sources 339 (2017) 68–79, https://doi.org/10.1016/j.jpowsour.2016.11.041.

[13] N.H. Othman, Z. Wu, K. Li, An oxygen permeable membrane microreactor with an in-situ deposited Bi1.5Y0.3Sm0.2O3-δ catalyst for oxidative coupling of methane, J. Membr. Sci. 488 (2015) 182–193, https://doi.org/10.1016/j.memsci.2015.04.027.

[14] F. Liang, H. Luo, K. Partovi, O. Ravkina, Z. Cao, Y. Liu, J. Caro, A novel CO2-stable dual phase membrane with high oxygen permeability, Chem. Commun. 50 (2014) 2451–2454, https://doi.org/10.1039/c3cc47962e.

[15] F. Schulze-Küppers, U.V. Unije, H. Blank, M. Balaguer, S. Baumann, R. Mücke, W. A. Meulenberg, Comparison of freeze-dried and tape-cast support microstructure on high-flux oxygen transport membrane performance, J. Membr. Sci. 564 (2018) 218–226, https://doi.org/10.1016/j.memsci.2018.07.028.

[16] X. Tan, Y. Liu, K. Li, Preparation of LSCF ceramic hollow-fiber membranes for oxygen production by a phase-inversion/sintering technique, Ind. Eng. Chem. Res. 44 (2005) 61–66, https://doi.org/10.1021/ie040179c.

[17] P. Niehoff, S. Baumann, F. Schulze-Küppers, R.S. Bradley, I. Shapiro, W. A. Meulenberg, P.J. Withers, R. Vaßen, Oxygen transport through supported Ba0.5Sr0.5Co 0.8Fe0.2O3-δ membranes, Separ. Purif. Technol. 121 (2014) 60–67, https://doi.org/10.1016/j.seppur.2013.07.002.

[18] S. Cheng, H. Huang, S. Ovtar, S.B. Simonsen, M. Chen, W. Zhang, M. Søgaard, A. Kaiser, P.V. Hendriksen, C. Chen, High-performance microchanneled asymmetric Gd0.1Ce0.9O1.95-δ-La0.6Sr0.4FeO3-δ-Based membranes for oxygen separation, ACS Appl. Mater. Interfaces 8 (2016) 4548–4560, https://doi.org/10.1021/acsami.5b10714.

[19] C. Gaudillere, J. Garcia-Fayos, J.M. Serra, Enhancing oxygen permeation through hierarchically-structured perovskite membranes elaborated by freeze-casting, J. Mater. Chem. A. 2 (2014) 3828, https://doi.org/10.1039/c3ta14069e.

[20] F. Schulze-Küppers, S. Baumann, W.A. Meulenberg, D. Stöver, H.-P. Buchkremer, Manufacturing and performance of advanced supported Ba0.5Sr0.5Co0.8Fe0.2O3-δ (BSCF) oxygen transport membranes, J. Membr. Sci. 433 (2013), https://doi.org/10.1016/j.memsci.2013.01.028.

[21] F. Schulze-Küppers, S. Baumann, W.A. Meulenberg, H.J.M. Bouwmeester, Influence of support layer resistance on oxygen fluxes through asymmetric membranes based on perovskite-type oxides SrTi<inf>1-x</inf>Fe<inf>x</inf>O<inf>3-δ</inf>, J. Membr. Sci. $_{596}$ (2020), 117704, https://doi.org/10.1016/j.memsci.2019.117704.

[22] R.K. Nishihora, P.L. Rachadel, M.G.N. Quadri, D. Hotza, Manufacturing porous ceramic materials by tape casting—a review, J. Eur. Ceram. Soc. 38 (2018) 988–1001, https://doi.org/10.1016/j.jeurceramsoc.2017.11.047.

[23] F. Schulze-Küppers, S. Baumann, F. Tietz, H.J.M. Bouwmeester, W.A. Meulenberg, Towards the fabrication of La0.98-xSrxCo0.2Fe0.8O3-δ perovskite-type oxygen transport membranes, J. Eur. Ceram. Soc. 34 (2014) 3741–3748, https://doi.org/10.1016/j.jeurceramsoc.2014.06.012.

[24] S. Baumann, J.M. Serra, M.P. Lobera, S. Escolástico, F. Schulze-Küppers, W. A. Meulenberg, Ultrahigh oxygen permeation flux through supported Ba0.5Sr0.5Co0.8Fe0.2O3-δ membranes, J. Membr. Sci. 377 (2011), https://doi.org/10.1016/j.memsci.2011.04.050.

[25] Y. Zhang, K. Zhou, J. Zeng, D. Zhang, Control of pore structures and sizes in freeze cast ceramics, Adv. Appl. Ceram. 112 (2013) 405–411, https://doi.org/10.1179/1743676113Y.0000000100.

[26] T. Liu, Y. Chen, S. Fang, L. Lei, Y. Wang, C. Ren, F. Chen, A dual-phase bilayer oxygen permeable membrane with hierarchically porous structure fabricated by freeze-drying tape-casting method, J. Membr. Sci. 520 (2016) 354–363, https://doi.org/10.1016/j.memsci.2016.07.046.

[27] T. Liu, W. Zhao, Y. Wang, Robust freeze-cast bilayer dual-phase oxygen transport membrane targeting chemical reactor application, ACS Appl. Nano Mater. 1 (2018) 3774–3778, https://doi.org/10.1021/acsanm.8b00990.

[28] T. Liu, L. Lei, J. Gu, Y. Wang, L. Winnubst, C. Chen, C. Ye, F. Chen, Enhanced water desalination performance through hierarchically-structured ceramic membranes, J. Eur. Ceram. Soc. 37 (2017) 2431–2438, https://doi.org/10.1016/j.jeurceramsoc.2017.02.001.

[29] W. He, H. Huang, J. fen Gao, L. Winnubst, C. sheng Chen, Phase-inversion tape casting and oxygen permeation properties of supported ceramic membranes,

J. Membr. Sci. 452 (2014) 294–299, https://doi.org/10.1016/j.memsci.2013.09.063.
[30] H. Huang, S. Cheng, J. Gao, C. Chen, J. Yi, Phase-inversion tape-casting preparation and significant performance enhancement of Ce0.9Gd0.1O1.95-La0.6Sr0.4Co0.2Fe0.8O3-?? dual-phase asymmetric membrane for oxygen separation, Mater. Lett. 137 (2014) 245–248, https://doi.org/10.1016/j.matlet.2014.09.016.
[31] N. Shi, F. Su, D. Huan, Y. Xie, J. Lin, W. Tan, R. Peng, C. Xia, C. Chen, Y. Lu, Performance and DRT analysis of P-SOFCs fabricated using new phase inversion combined tape casting technology, J. Mater. Chem. A. 5 (2017) 19664–19671, https://doi.org/10.1039/c7ta04967f.
[32] Y. Meng, W. He, X. xiang Li, J. Gao, Z. Zhan, J. Yi, C. Chen, H.J.M. Bouwmeester, Asymmetric La0.6Sr0.4Co0.2Fe0.8O3-Δ membrane with reduced concentration polarization prepared by phase-inversion tape casting and warm pressing, J. Membr. Sci. 533 (2017) 11–18, https://doi.org/10.1016/j.memsci.2017.03.025.
[33] T. Liu, Y. Wang, Y. Zhang, S. Fang, L. Lei, C. Ren, F. Chen, Steam electrolysis in a solid oxide electrolysis cell fabricated by the phase-inversion tape casting method, Electrochem. Commun. 61 (2015) 106–109, https://doi.org/10.1016/j.elecom.2015.10.015.
[34] C.D. Bird, N.J. Emery, Insightful problem solving and creative tool modification by captive nontool-using rooks, Proc. Natl. Acad. Sci. Unit. States Am. 106 (2009) 10370–10375, https://doi.org/10.1073/pnas.0901008106.
[35] N.H. Othman, Z. Wu, K. Li, A micro-structured La0.6Sr0.4Co0.2Fe0.8O3-δ hollow fibre membrane reactor for oxidative coupling of methane, J. Membr. Sci. 468 (2014) 31–41, https://doi.org/10.1016/j.memsci.2014.05.051.
[36] J. jun Liu, T. Liu, W. dong Wang, J. feng Gao, C. sheng Chen, Zr 0.84Y 0.16O 1.92-La 0.8Sr 0.2Cr 0.5Fe 0.5O 3-δ dual-phase composite hollow fiber membrane targeting chemical reactor applications, J. Membr. Sci. 389 (2012) 435–440, https://doi.org/10.1016/j.memsci.2011.11.010.
[37] X. Shao, Z. Wang, S. Xu, K. Xie, X. Hu, D. Dong, G. Parkinson, C.Z. Li, Microchannel structure of ceramic membranes for oxygen separation, J. Eur. Ceram. Soc. 36 (2016) 3193–3199, https://doi.org/10.1016/j.jeurceramsoc.2016.05.005.
[38] Y. Zhang, R.H. Yuan, J.F. Gao, C.S. Chen, Oxygen permeation properties of supported planar Zr0.84Y0.16O1.92-La0.8Sr0.2Cr0.5Fe0.5O3-δ composite membranes, Separ. Purif. Technol. 166 (2016) 142–147, https://doi.org/10.1016/j.seppur.2016.04.029.
[39] J. Suntivich, K.J. May, H.A. Gasteiger, J.B. Goodenough, Y. Shao-Horn, A perovskite oxide optimized for oxygen evolution catalysis from molecular orbital principles, Science 334 (2011) 1383–1385, https://doi.org/10.1126/science.1212858 (80-).
[40] Z. Shao, S.M. Haile, A high-performance cathode for the next generation of solid-oxide fuel cells, Nature 431 (2004) 170–173, https://doi.org/10.1038/nature02863.
[41] W. Zhou, R. Ran, Z. Shao, Progress in understanding and development of Ba0.5Sr0.5Co0.8Fe0.2O3-δ-based cathodes for intermediate-temperature solid-oxide fuel cells: a review, J. Power Sources 192 (2009) 231–246, https://doi.org/10.1016/j.jpowsour.2009.02.069.
[42] O. Ravkina, T. Klande, A. Feldhoff, Investigation of Zr-doped BSCF perovskite membrane for oxygen separation in the intermediate temperature range, J. Solid State Chem. 201 (2013) 101–106, https://doi.org/10.1016/j.jssc.2013.02.023.
[43] M. Meffert, P. Müller, H. Störmer, L.S. Unger, C. Niedrig, S.F. Wagner, S. Saher, H. Bouwmeester, E. Ivers-Tiffée, D. Gerthsen, Effect of yttrium (Y) and zirconium (Zr) doping on the thermodynamical stability of the cubic Ba0.5Sr0.5Co0.8Fe0.2O3-δ phase, Microsc. Microanal. 20 (2014) 466–467, https://doi.org/10.1017/S143192761400405X.
[44] L. Navarrete, C. Hannahan, J.M. Serra, Intermediate Temperature Solid-Oxide Cells 376, 2022, pp. 2–10.
[45] C.A. Smolders, A.J. Reuvers, R.M. Boom, I.M. Wienk, Microstructures in phase-inversion membranes. Part 1. Formation of macrovoids, J. Membr. Sci. 73 (1992) 259–275, https://doi.org/10.1016/0376-7388(92)80134-6.
[46] L. Wang, R. Merkle, J. Maier, Surface Kinetics and Mechanism of Oxygen Incorporation into Ba[sub 1−x]Sr[sub x]Co[sub y]Fe[sub 1−y]O[sub 3−δ] SOFC Microelectrodes, J. Electrochem. Soc. 157 (2010) B1802, https://doi.org/10.1149/1.3494224.
[47] H.J.M. Bouwmeester, A.J. Burggraaf, Dense ceramic membranes for oxygen separataion, in: L. Burggraaf, A.J. Cot (Eds.), Fundam. Inorg. Membr. Sci. Technol., Elsevier B.V, 1996, pp. 435–528.
[48] A. Häffelin, C. Niedrig, S.F. Wagner, S. Baumann, W.A. Meulenberg, E. Ivers-Tiffée, Three-dimensional performance model for oxygen transport membranes, J. Electrochem. Soc. 161 (2014), https://doi.org/10.1149/2.0601414jes.
[49] S. Baumann, P. Niehoff, F. Schulze-Küppers, M. Ramasamy, W.A. Meulenberg, O. Guillon, The role of solid-gas electrochemical interfaces for mixed ionic electronic conducting oxygen transport membranes, in: ECS Trans, 2015, https://doi.org/10.1149/06602.0021ecst.
[50] X. Chang, C. Zhang, Z. Wu, W. Jin, N. Xu, Contribution of the surface reactions to the overall oxygen permeation of the mixed conducting membranes, Ind. Eng. Chem. Res. 45 (2006) 2824–2829, https://doi.org/10.1021/ie051162c.
[51] R.H.E. van Doorn, I.C. Fullatron, R.A. De Souza, J.A. Kilner, H.J.M. Bouwmeester, A.J. Burggraaf, Surface oxygen exchange of La03Sr07CoO2-d, Solid State Ionics 96 (1997) 1–7.